STRUCTURAL SCIENCE
CRYSTAL ENGINEERING
MATERIALS

Volume 76 (2020)

Supporting information for article:

Ca-doped rare earth perovskite materials for tailored exsolution of metal nanoparticles

Lorenz Lindenthal, Thomas Ruh, Raffael Rameshan, Harald Summerer, Andreas Nenning, Christopher Herzig, Stefan Löffler, Andreas Limbeck, Alexander Karl Opitz, Peter Blaha and Christoph Rameshan

S1. Experiments on Doping the B-site with Ni

Besides Co, using Ni as a dopant for the perovskite B-site was attempted. For this reason, the two materials $Nd_{0.6}Ca_{0.4}Fe_{0.9}Ni_{0.1}O_{3-\delta}$ (NdNi0.1) and $Nd_{0.6}Ca_{0.4}Fe_{0.95}Ni_{0.05}O_{3-\delta}$ (NdNi0.05) were additionally synthesised. The diffractograms of the B-site doped perovskites, together with the one of Nd0.6 for comparison, are shown in Figure S1. They are all very similar. All the Bragg peaks visible for Nd0.6 appear also for the other samples, at nearly the same positions and with similar intensities. The peaks of the doped materials were slightly narrower; thus, some peaks were better resolved. This indicated larger crystallites (larger coherent regions for diffraction and thus more ideal Bragg peaks) in the doped perovskites than in Nd0.6.

In the diffractogram of NdCo, no additional peaks could be observed, confirming the phase purity of the material. On the contrary, the Ni doped perovskites were not phase pure. Small additional peaks at 2θ of 37.3°, 43.4° and 63.0° appeared. These peaks could be assigned to NiO. These results showed that a 10 % doping with Ni was not suitable, as not all Ni could be incorporated into the perovskite lattice, instead forming an additional phase. Therefore, NdNi0.05 was synthesised, with the hope that the lower amount of 5 % Ni would be incorporated fully. However, the NiO peaks were still visible for NdNi0.05, although with lower intensities. Thus, this sample was not phase pure as well, only the amount of excess NiO was lower.

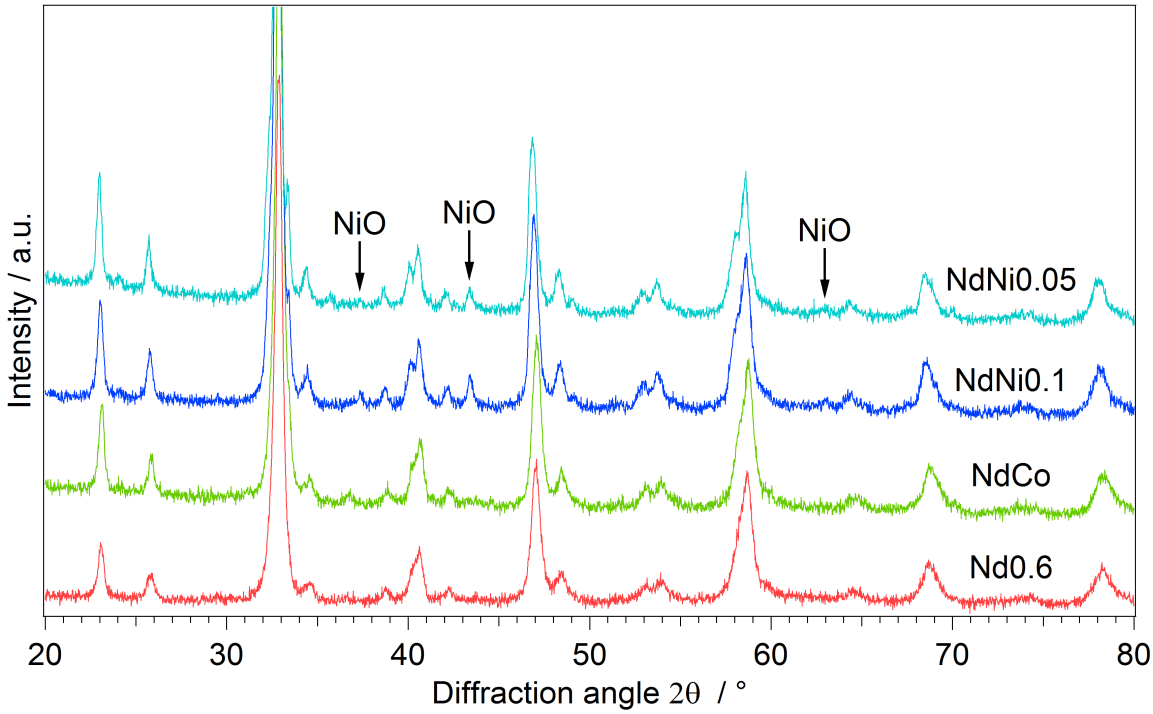

Figure S1 Diffractograms of the samples with B-site doping and of Nd0.6, for comparison. They all looked very similar, indicating equivalent structures. Only for the samples with Ni doping additional Bragg peaks occurred, which could be assigned to NiO. These samples were not phase pure.

One possible explanation why doping with Ni proved to be difficult, could be based on the oxidation state of the B-site cations necessary to establish charge balance in the perovskite. The oxidation state of the B-site cations in the investigated perovskite materials was usually +3 or +4. The amount of the latter increased with the amount of Ca doping. These oxidation states are common for Fe, and also possible for Co. On the other hand, Ni mostly occurs in the oxidation state +2 and reaching an oxidation state of +3, or even +4, is difficult. Therefore, Ni could be incorporated only partly into the perovskite phase, while the excessive Ni formed a segregated NiO phase.

This segregation could also be observed with SEM/EDX. An EDX mapping was performed on the 10% Ni doped sample (Figure S2). The Ni content was characterised by the net intensity of the Ni L peak in the EDX spectra. It could be seen that Ni was not distributed homogeneously, but was rather concentrated to some specific spots. The occurrence of a more Ni rich region did not coincide with any feature in the secondary electron image, possibly meaning that the NiO was not located directly at the surface.

After the unsuccessful attempt of synthesising a phase pure Ni doped perovskite, it was decided to focus on the other samples within the scope of this paper.

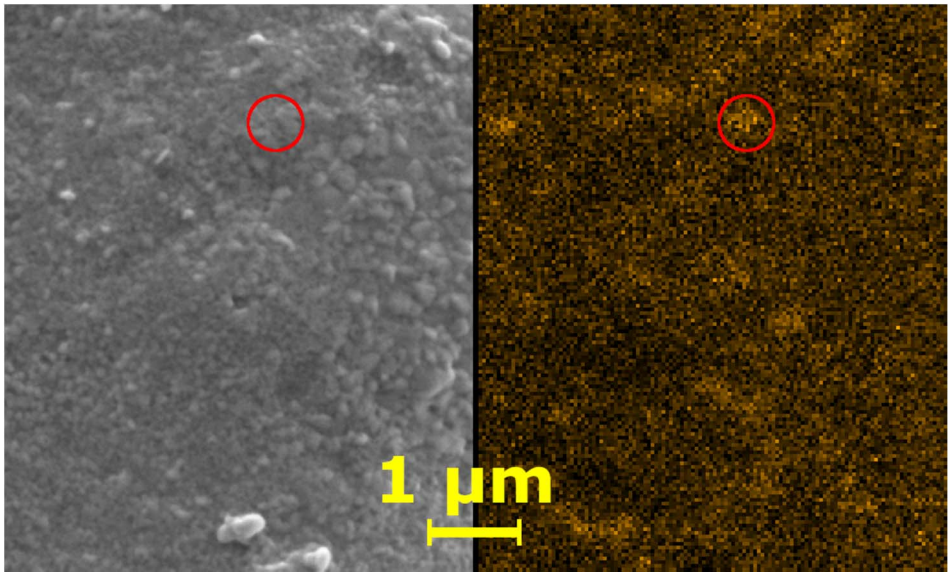

Figure S2 SEM image (secondary electrons) of the pristine sample with 10% Ni doping, collected at an accelerating voltage of 5 kV, and distribution of Ni in the same area using EDX (spectra collected with 10 kV accelerating voltage). The Ni content was characterised by the net intensity of the Ni L peak (the brighter the orange colour, the higher the peak). Ni was not distributed homogeneously, but in the secondary electron image no signs of inhomogeneity were visible. The red circle marks a more Ni rich region as an example, while in the left image there was no observable difference to the surrounding regions.

S2. ICP-OES Experimental Details and Results

To determine the actual composition of the synthesised samples, inductively coupled plasma-optical emission spectroscopy (ICP-OES) was used. Therefore, aliquots of 30–40 mg of the solid powder were digested in 10 mL polypropylene tubes with 0.5 mL of concentrated Hydrochloric acid (37 % w/w, HCl, EMSURE®). After dissolution at room temperature, the sample volume was increased to 9 mL by addition of ultrapure water and subsequently diluted 1/50 to reach the final concentration. For all dilutions 1 % (v/v) HCl containing 1 µg g^{-1} europium (Eu, Certipur®, Merck, Germany) as internal standard was used. Three replicates of each sample were digested and used for measurement.

Single element standards for iron (Fe, Certipur®, Merck, Germany), calcium (Ca, Fluka Analytical, Sigma Aldrich, St. Louis, MO, USA), neodymium (Nd, BDH Laboratory Supplies, Pool, England), nickel (Ni), cobalt (Co) and lanthanum (La, Prolabo®, VWR, Leiceister, England) were mixed and standard solutions with concentration levels ranging from 0.5 to 20 µg g^{-1} were prepared using the same diluted HCl as for the samples.

Samples and standards were analysed with an iCAP 6500 ICP-OES spectrometer (Thermo Scientific, USA) equipped with a Meinhardt nebulizer and a cyclonic spray chamber (Glass Expansion, Port Melbourne, Australia). Sample-uptake was achieved with the peristaltic pump of the instrument. Background-corrected emission signals were recorded in the radial viewing mode and processed using Qtegra software (Thermo Scientific, USA). Four replicates with an integration time of 8 s each were measured for samples as well as standard solutions. The optimized ICP-OES parameters as well as the monitored emission lines are summarized in Table S1. For each element two to three intense but non interfered emission lines were measured.

Observed signal intensities were normalized using the signal response for the internal standard (Eu), and finally converted into concentration units by means of external aqueous calibration. By using the molar masses of each element, the mole fractions of the cations present in the investigated samples were calculated. Derived Eu signals were constant over each measurement session (less than 5% relative standard deviation for the whole measurement period, indicating the absence of temporal trends), and no significant difference in Eu-response between samples and calibration standards was observed.

The results of the determination of the real stoichiometry of the samples by ICP-OES are summarized in Table S2.

Table S1 Optimized ICP-OES parameters used for the measurements.

RF power	1200 W
exposure time	8 s

nebulizer gas flow	0.7 L min^{-1} argon
cooling gas flow	12 L min^{-1} argon
auxiliary gas flow	0.8 L min^{-1} argon
viewing height above load-coil	12 mm
Spectral range	Visible

Elements	Emission line [nm]
Fe	259.94*, 238.20, 240.49
Nd	401.23*, 406.11, 430.36,
Ca	393.37, 422.67, 373.69*
Co	228.89*, 228.62, 237.96
Ni	221.65*, 231.60, 352.45
La	333.75*, 412.32, 379.47
Eu	412.97*, 420.51

Emission lines marked with * used for evaluation

Table S2 Results of the determination of the stoichiometry of various samples by ICP-OES normalised to the B-site. It is not possible to measure the oxygen content with the applied method. Furthermore, it depends on the oxidation state of the sample. Thus, the oxygen stoichiometry is denoted $O_{3-\delta}$. The real stoichiometry agrees mostly well with the stoichiometry that has been aimed at during synthesis. The A-site occupation is slightly sub stoichiometric; this effect is stronger with Nd than with La.

Sample	Nominal	Stoichiometry by ICP-OES
La0.9	$La_{0.9}Ca_{0.1}FeO_{3-\delta}$	$La_{0.87}Ca_{0.09}FeO_{3-\delta}$
La0.6	$La_{0.6}Ca_{0.4}FeO_{3-\delta}$	$La_{0.59}Ca_{0.38}FeO_{3-\delta}$
Nd0.9	$Nd_{0.9}Ca_{0.1}FeO_{3-\delta}$	$Nd_{0.82}Ca_{0.08}FeO_{3-\delta}$
Nd0.6	$Nd_{0.6}Ca_{0.4}FeO_{3-\delta}$	$Nd_{0.54}Ca_{0.37}FeO_{3-\delta}$
NdCo	$Nd_{0.6}Ca_{0.4}Fe_{0.9}Co_{0.1}O_{3-\delta}$	$Nd_{0.54}Ca_{0.38}Fe_{0.9}Co_{0.1}O_{3-\delta}$

S3. Structural Characterisation

Table S3 Experimental details for the powder diffraction experiment with the La0.9-sample.

La09Ca01FeO3

Crystal data	
Chemical formula	$La_{0.9}Ca_{0.1}FeO_3$
M_r	232.87
Crystal system, space group	Orthorhombic, *Pnma*
Temperature (K)	295
a, *b*, *c* (Å)	5.558528, 7.837216, 5.547272
V (Å^3)	241.66
Z	4
Radiation type	Cu $K\alpha_{1+2}$, λ = 1.540598 Å
Data collection	
Diffractometer	PANalytical X'Pert Pro
Specimen mounting	Si single crystal
Data collection mode	Reflection
Scan method	Step
2θ values (°)	$2\theta_{min}$ = 15.00 $2\theta_{max}$ = 119.96 $2\theta_{step}$ = 0.02
Refinement	
R factors and goodness of fit	R_p = 0.029, R_{wp} = 0.039, R_{exp} = 0.024, R_{Bragg} = 0.046, χ^2 = 2.575

Computer programs: HighScore Plus 4.8.0.

Table S4 Experimental details for the powder diffraction experiment with the La0.6-sample.

	La06Ca04FeO3
Crystal data	
Chemical formula	$La_{0.6}Ca_{0.4}FeO_3$
M_r	203.22
Crystal system, space group	Orthorhombic, *Pnma*
Temperature (K)	295
a, *b*, *c* (Å)	5.506428, 7.776180, 5.529845
V (Å^3)	236.78
Z	4
Radiation type	Cu $K\alpha_{1+2}$, λ = 1.540598 Å
Data collection	
Diffractometer	PANalytical X'Pert Pro
Specimen mounting	Si single crystal
Data collection mode	Reflection
Scan method	Step
2θ values (°)	$2\theta_{min}$ = 15.00 $2\theta_{max}$ = 119.96 $2\theta_{step}$ = 0.02
Refinement	
R factors and goodness of fit	R_p = 0.023, R_{wp} = 0.031, R_{exp} = 0.021, R_{Bragg} = 0.037, χ^2 = 2.197

Computer programs: HighScore Plus 4.8.0.

Table S5 Experimental details for the powder diffraction experiment with the Nd0.9-sample.

	Nd09Ca01FeO3
Crystal data	
Chemical formula	$Nd_{0.9}Ca_{0.1}FeO_3$
M_r	237.67
Crystal system, space group	Orthorhombic, *Pnma*
Temperature (K)	295
a, *b*, *c* (Å)	5.568011, 7.756535, 5.451495
V (Å^3)	235.44
Z	4
Radiation type	Cu *K*α$_{1+2}$, λ = 1.540598 Å
Data collection	
Diffractometer	PANalytical X'Pert Pro
Specimen mounting	Si single crystal
Data collection mode	Reflection
Scan method	Step
2θ values (°)	$2\theta_{min}$ = 15.00 $2\theta_{max}$ = 116.98 $2\theta_{step}$ = 0.02
Refinement	
R factors and goodness of fit	R_p = 0.027, R_{wp} = 0.035, R_{exp} = 0.025, R_{Bragg} = 0.043, χ^2 = 1.894

Computer programs: HighScore Plus 4.8.0.

Table S6 Experimental details for the powder diffraction experiment with the Nd0.6-sample.

	Nd06Ca04FeO3
Crystal data	
Chemical formula	$Nd_{0.6}Ca_{0.4}FeO_3$
M_r	206.42
Crystal system, space group	Orthorhombic, *Pnma*
Temperature (K)	295
a, *b*, *c* (Å)	5.533425, 7.725984, 5.448728
V (Å^3)	232.94
Z	4
Radiation type	Cu *K*α$_{1+2}$, λ = 1.540598 Å
Data collection	
Diffractometer	PANalytical X'Pert Pro
Specimen mounting	Si single crystal
Data collection mode	Reflection
Scan method	Step
2θ values (°)	$2\theta_{min}$ = 15.00 $2\theta_{max}$ = 116.98 $2\theta_{step}$ = 0.02
Refinement	
R factors and goodness of fit	R_p = 0.024, R_{wp} = 0.030, R_{exp} = 0.026, R_{Bragg} = 0.011, χ^2 = 1.375

Computer programs: HighScore Plus 4.8.0.

Table S7 **Cell parameters of the used starting structures (a_{init}, b_{init}, c_{init}) compared to the final parameters after refinement (a_{end}, b_{end}, c_{end}).**

Sample	Starting Structure	a_{init} / Å	b_{init} / Å	c_{init} / Å	a_{end} / Å	b_{end} / Å	c_{end} / Å
La0.9	#01-082-9272	5.530	7.824	5.539	5.559	7.837	5.547
La0.6	#04-017-9772	5.500	7.776	5.501	5.506	7.776	5.530
Nd0.9	#04-014-5430	5.545	7.763	5.589	5.568	7.757	5.451
Nd0.6	#04-014-5430	5.545	7.763	5.589	5.533	7.726	5.449

Table S8 **Glazer angles of the used starting structures (a_{init}, b_{init}) compared to the final angles after refinement (a_{end}, b_{end}).**

Sample	Starting Structure	a_{init} / °	b_{init} / °	a_{end} / °	b_{end} / °
La0.9	#01-082-9272	7.57	8.08	7.47	8.69
La0.6	#04-017-9772	7.74	7.75	8.16	8.66
Nd0.9	#04-014-5430	10.12	7.00	10.18	8.73
Nd0.6	#04-014-5430	10.12	7.00	10.84	6.22

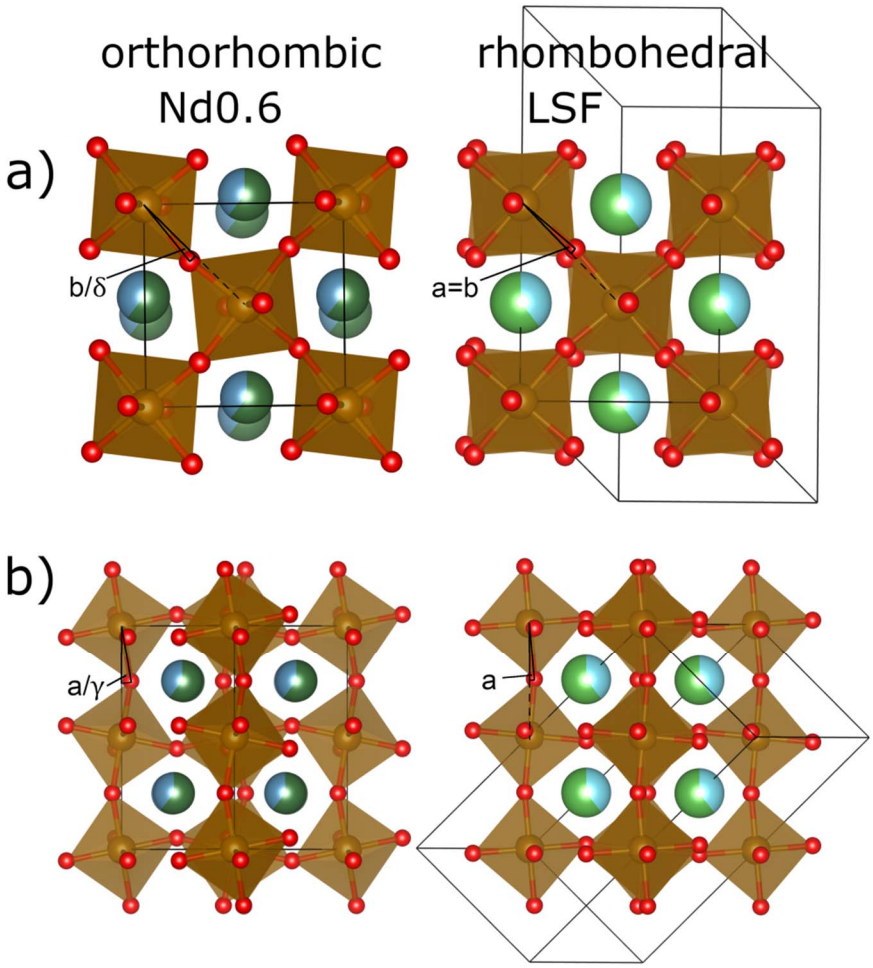

Figure S3 Comparison of the structures of the orthorhombic Nd0.6 and the rhombohedral LSF. View a) **is along the [010] direction (b-axis)** of the orthorhombic unit cell of Nd0.6, view b) is along the **[101] direction**. **Note that t**he equivalent views for the rhombohedral structure do not coincide with the **same crystallographic directions**. The marked **Glazer** angles **a** and **b (projected along the direction of the view)** were used to quantify the tilting of the octahedrons. **The angles γ and δ, used for DFT comparison, are the unprojected angles.**

The two possible symmetries of the perovskite lattice, orthorhombic and rhombohedral, are compared in Figure S3, exemplary with Nd0.6 and LSF. Two views are presented here, in the **[010]** direction (Figure S3a) and in the **[101]** direction (Figure S3b) of the orthorhombic unit cell. Equivalent views can be found in the rhombohedral structure, although they do not coincide with the **same crystallographic directions** in that case. It can be seen, that whereas the octahedrons are stacked directly on top of each other in the orthorhombic structure **(corresponding to the b^+ tilting of the Glazer system)** in Figure S3a, the A-site cations do not form straight rows in that direction. For the rhombohedral structure it is the other way round, with straight rows of A-site cations and two alternating positions of the octahedrons **(corresponding to an a^- tilt)**. In Figure S3b no such differences affecting the symmetry are observable. However, for both symmetries the alternate tilting

of the octahedrons can be seen very well **(again corresponding to an a⁻ tilt)**. This tilting is stronger in the orthorhombic structure, induced by the smaller A-site cations and the higher non-ideality.

S4. DFT Calculations

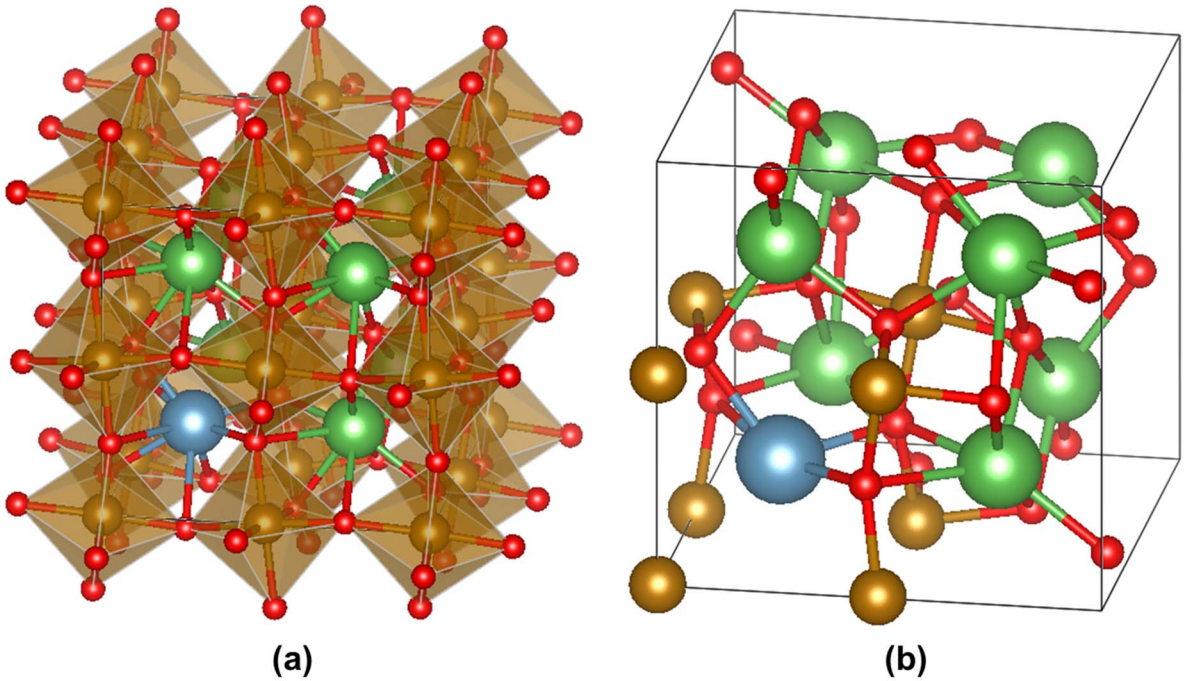

Figure S4 Model used for DFT calculations of $La_{0.875}Ca_{0.125}FeO_3$. In a) the network of tilted and slightly distorted Fe-O coordination octahedral is shown. The right part (b) depicts the unit cell with 40 atoms used for the calculations. Atom colors: La – green, Ca – blue, Fe – brown, O – red.

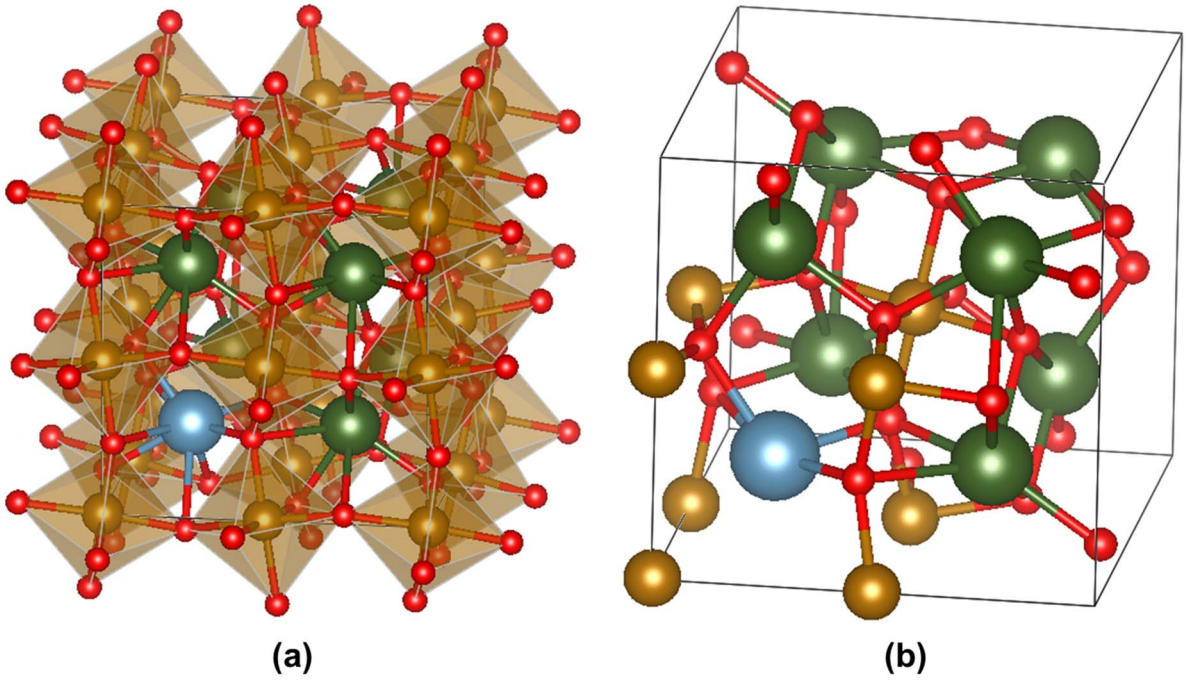

Figure S5 Model used for DFT calculations of $Nd_{0.875}Ca_{0.125}FeO_3$. In a) the network of tilted and slightly distorted Fe-O coordination octahedral is shown. The right part (b) depicts the unit cell with 40 atoms used for the calculations. Atom colors: Nd – green, Ca – blue, Fe – brown, O – red.

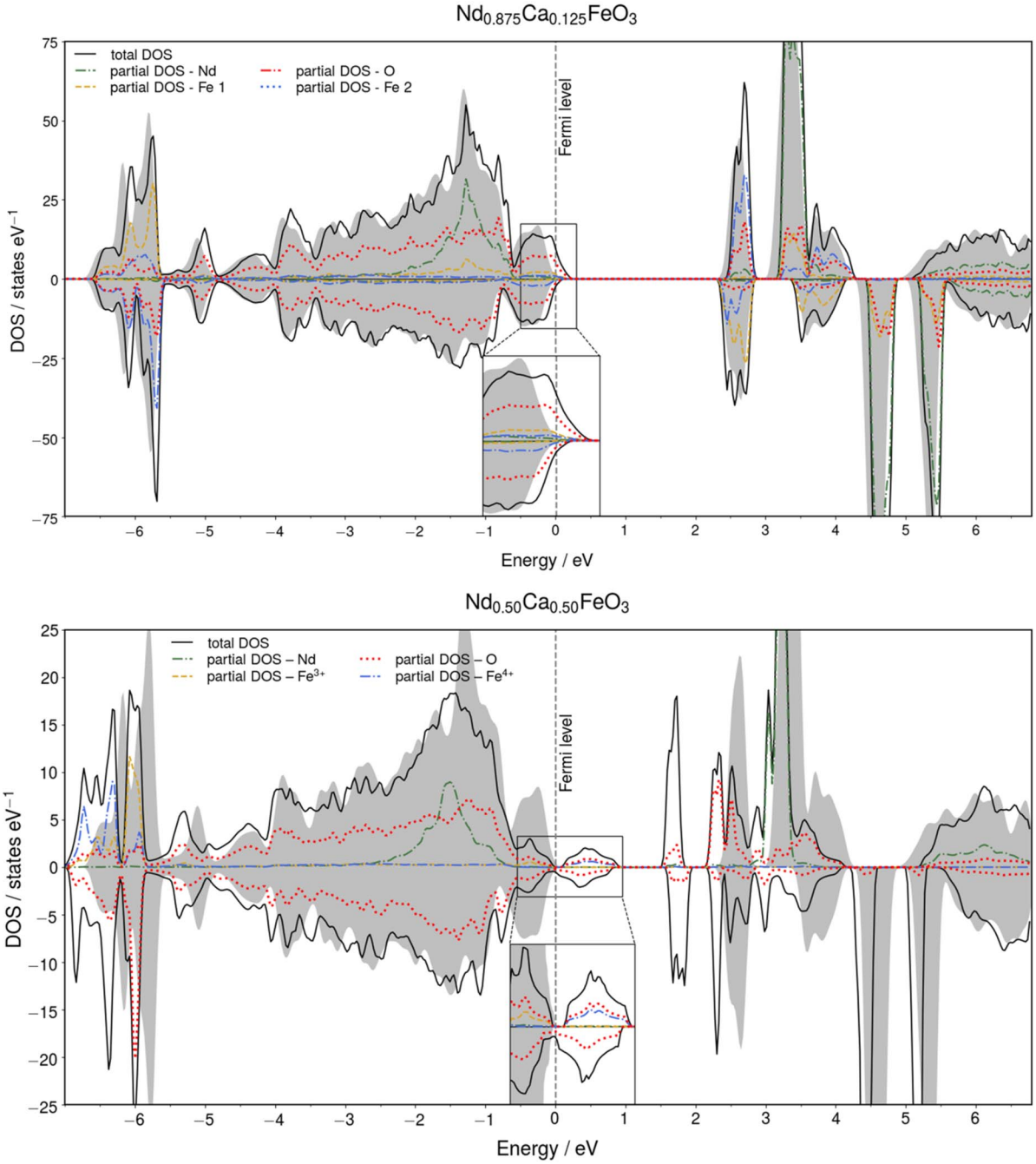

Figure S6 Total (black solid lines) and partial (dashed colored lines) DOS for $Nd_{0.875}Ca_{0.125}FeO_3$ (top) and for $Nd_{0.5}Ca_{0.5}FeO_3$ (bottom). The dashed vertical lines represent the Fermi levels (set to 0 eV). The total DOS for the bulk is shown as grey area as reference. The insets show the region around the Fermi level. States above the x-axis (positive values) correspond to states of spin-up electrons, while states below the x-axis (negative values) correspond to states of spin-down electrons. For Nd,

Fe^{3+}, and Fe^{4+} in the bottom figure only one spin is shown, the antiferromagnetic counterparts are omitted.

S5. Macroscopic Structure of the Ca-doped Perovskites

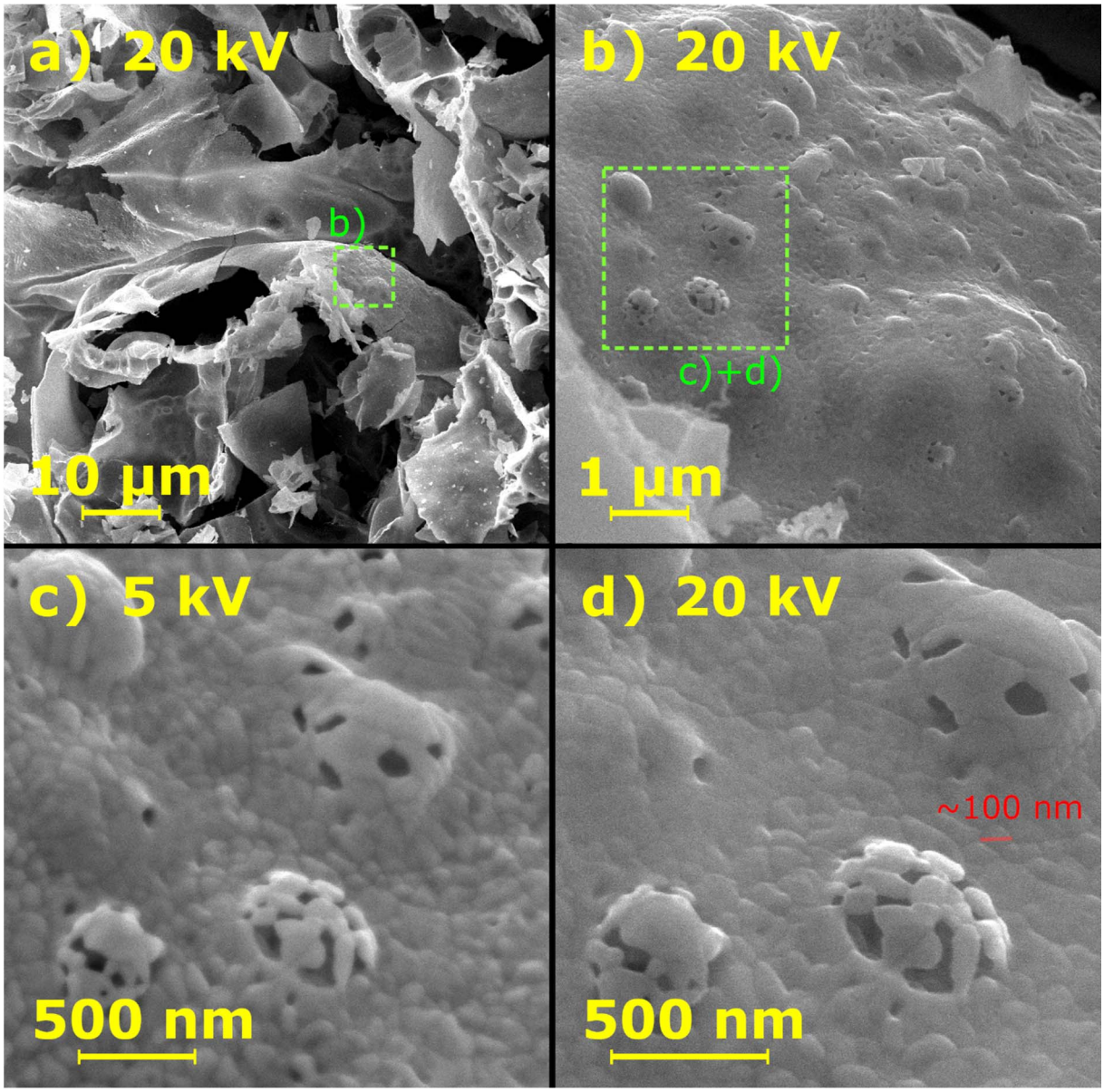

Figure S7 SEM images of a globular cavity in the pristine La0.9-sample with different magnifications and accelerating voltages. Image a) shows that the cavity has a slightly distorted spherical shape. The morphology of the wall can be seen in image b). It is built up from small crystallites, mostly densely grown together. Some holes in the structure coincide with the appearance of bumps. This is where gas has left the formed foam during synthesis. Images c) and d) exhibit details of these bumps. The influence of the accelerating voltage is observable here. In image c) with 5 kV, the topography and the round shape of the crystallites are better recognisable, because the

measurement is more surface sensitive. In image d) with 20 kV, the surface seems flatter, but a higher resolution could be achieved, enabling a more accurate estimation of the crystallite size – with diameters found to be around 100 nm.

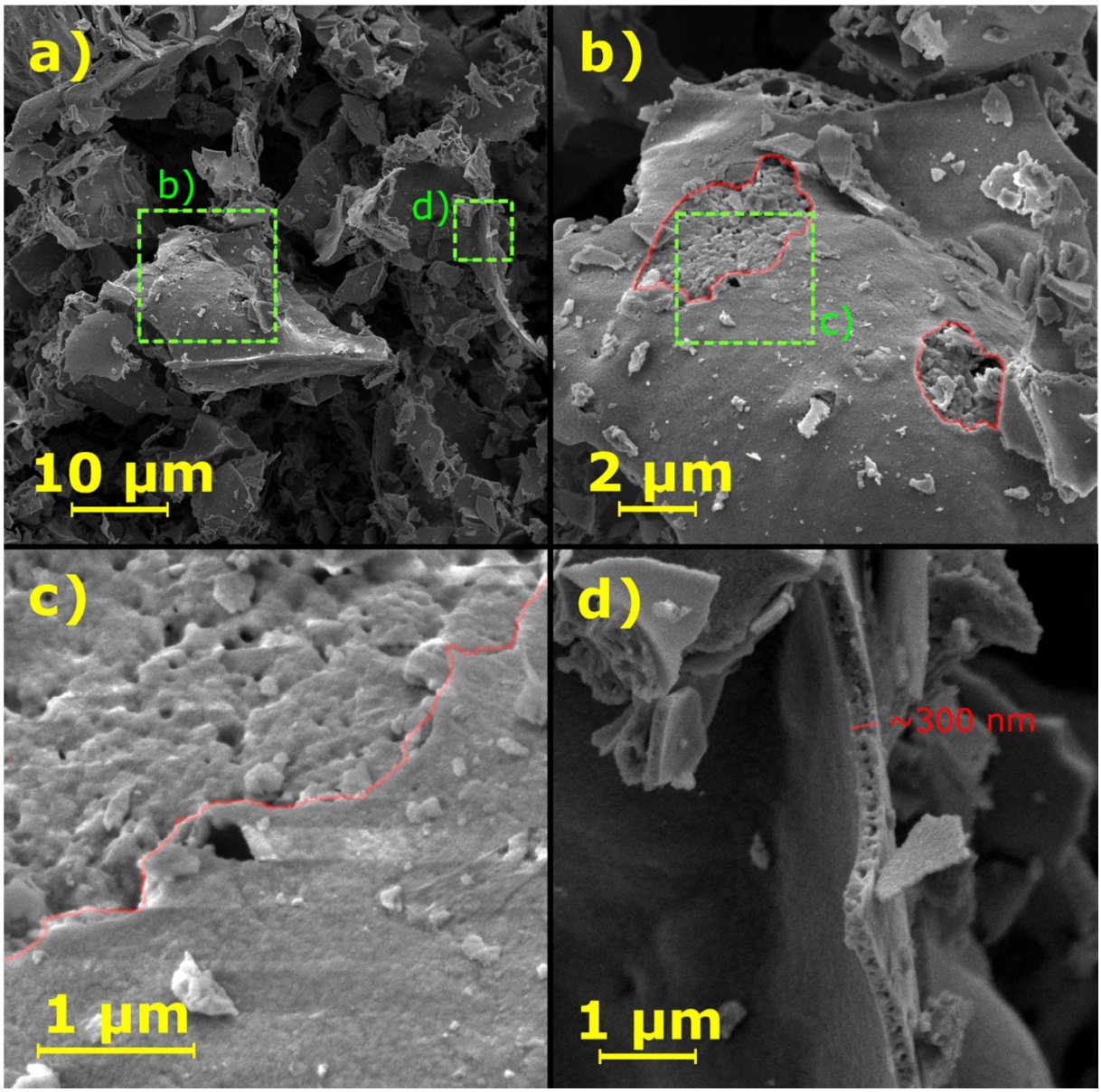

Figure S8 SEM images of the pristine La0.6-sample with different magnifications and the same accelerating voltage of 5 kV. Image a) reveals that the foam like morphology is very similar to that of the La0.9-sample. Images b) and c) display the surface of a cavity wall at higher magnifications. As in the La0.9-sample, it is mostly dense. Where the topmost layer is missing (regions with borders marked red), a more porous structure is visible. In addition, the crystallites that build up the walls are distinguishable in image c). This morphology of the cavity walls is also observable in Image d), a magnified section of a wall that is approximately 300 nm thick.

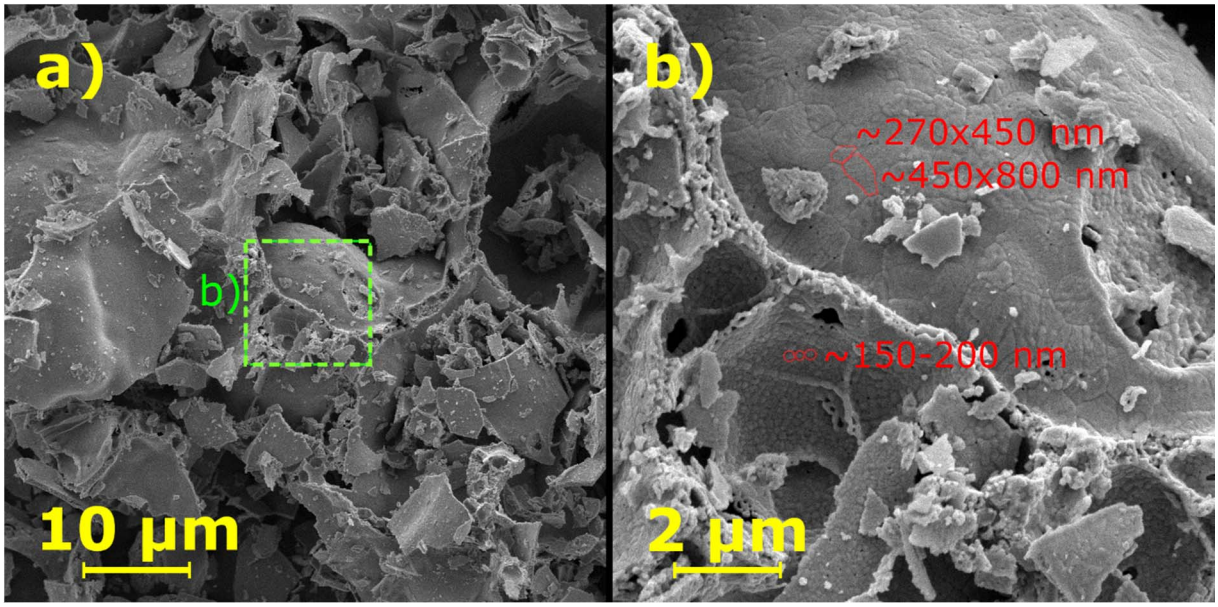

Figure S9 SEM images of the pristine Nd0.9-sample with different magnifications and the same accelerating voltage of 5 kV. Image a) reveals the foam like morphology as observed in the other samples. The crystallites of the material (marked with red border) that build up the cavity walls are visible in image b) at higher magnification. There are larger crystallites, which are flat at the surface, and smaller more globular ones. Both types are larger than the crystallites in the La0.9- or the La0.6-sample.

S6. Calculation of oxygen partial pressure $p(O_2)$

The oxygen partial pressure was calculated from the chemical equilibrium of the hydrogen oxidation reaction

$$H_2 + \frac{1}{2}O_2 \rightleftharpoons H_2O, \tag{1}$$

with the equilibrium constant

$$K = \frac{p(H_2O)}{\sqrt{p(O_2)}\,pH_2} = \exp\left(-\frac{\Delta_R G}{RT}\right). \tag{2}$$

There, $\Delta_R G^0$ is the Gibbs free energy of reaction 1, when all species have standard pressure of 1 atm, R and T are gas constant and temperature, respectively. The oxygen partial pressure is therefore calculated by the relation

$$p(O_2) = \frac{p(H_2O)^2}{p(H_2)^2}\exp\left(\frac{\Delta_R G}{RT}\right). \tag{3}$$

The (temperature dependent) value of $\Delta_R G^0$ is available online (NIST).

For the reduction conditions used in this study (H_2:H_2O = 32:1, 923 K), the corresponding partial pressure is $5.3 \cdot 10^{-26}$ bar.

S7. Characterisation of Exsolution Properties

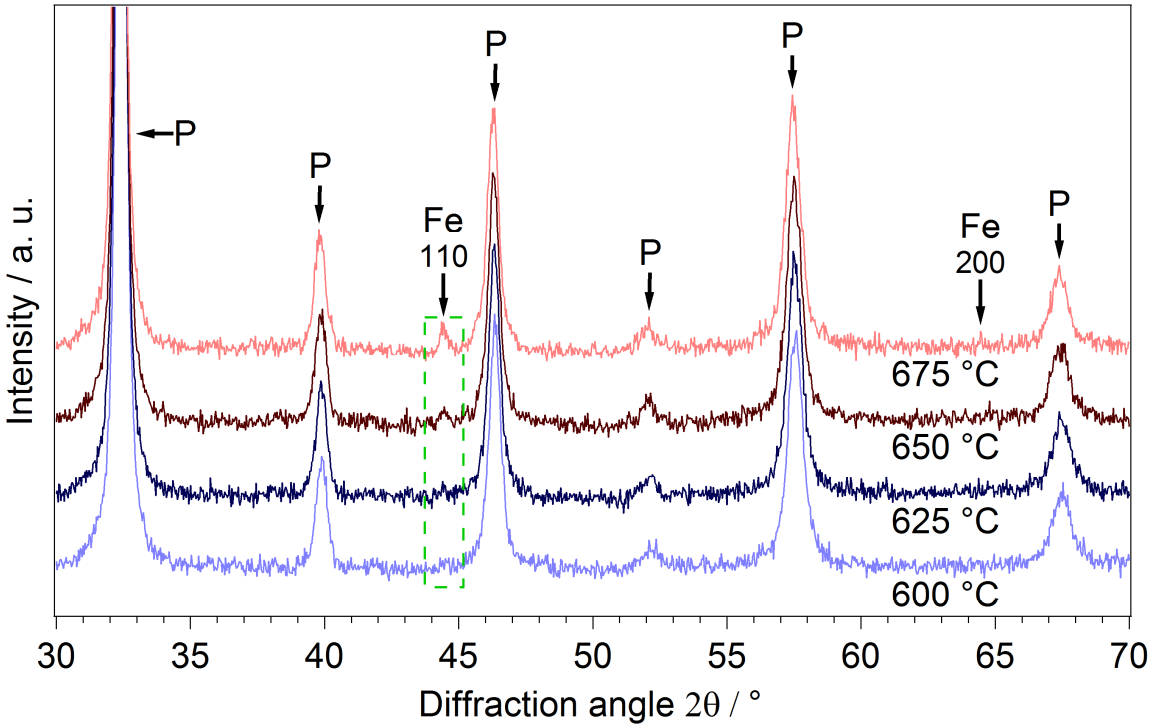

Figure S10 Diffractograms of the La0.6-sample during the reduction with wet H_2 at increasing temperatures. The perovskite structure (peaks labelled "P") stayed intact. The Fe peak (green border) appeared at 650 °C at 2θ of 44.4°.

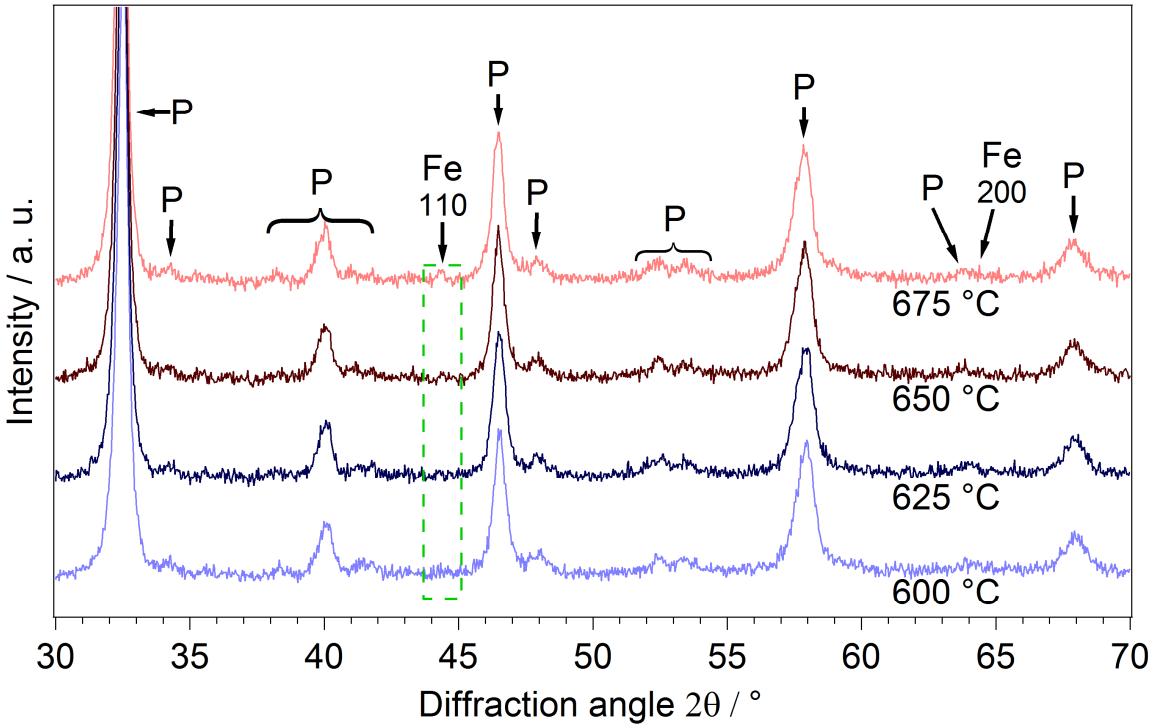

Figure S11 Diffractograms of the Nd0.6-sample during the reduction with wet H_2 at increasing temperatures. The perovskite structure (peaks labelled "P") was intact at all measured temperatures. Only at the highest temperature of 675 °C a small Fe peak (green border) appeared.

A further in situ XRD experiment was performed with the commercially available LSF (Figure S12). Here, exsolution of Fe (Bragg peak at 2θ of 44.5°) started already at 425 °C. The perovskite structure was intact and no segregation of a Sr containing phase could be observed over the whole temperature range (up to 500 °C, which is not shown here). The reduced samples after the XRD measurements were investigated with SEM. An image of the sample after the last temperature step at 500 °C is shown in Figure S13. Very small nanoparticles with diameters of around 20 nm can be seen, proving that exsolution took place.

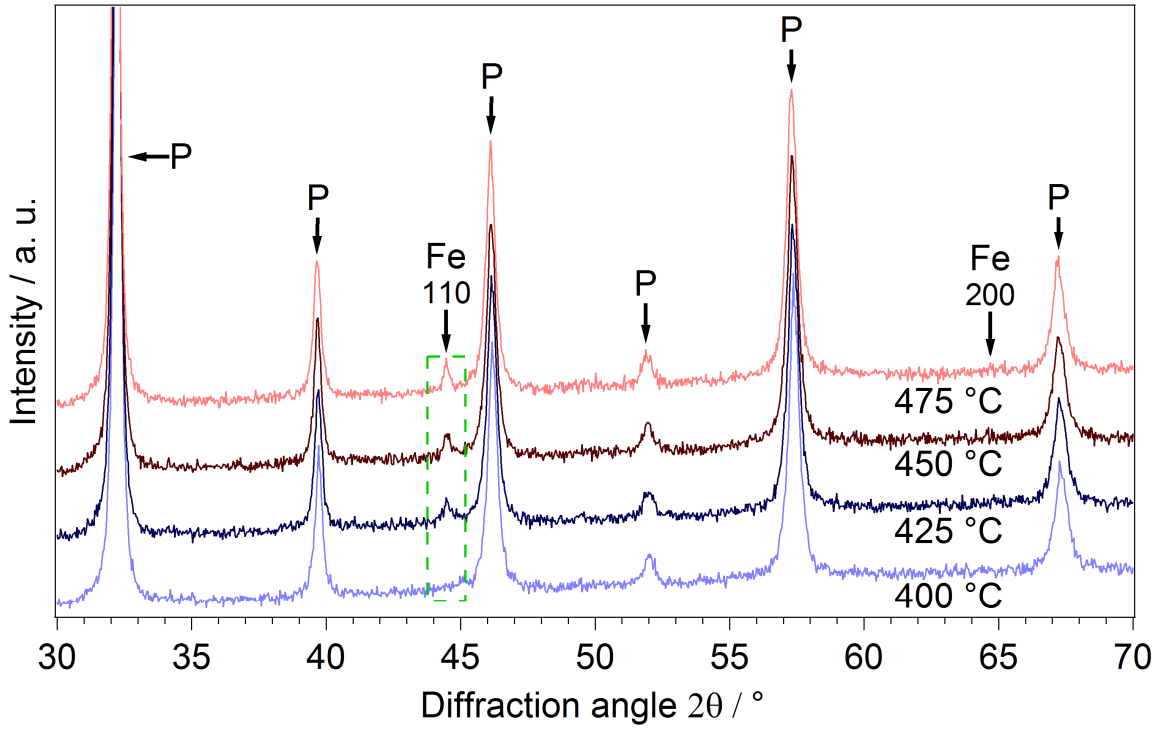

Figure S12 Diffractograms of the LSF-sample during the reduction with wet H_2 at increasing temperatures. At a temperature of 425 °C, elemental Fe (green border) started to appear. This temperature is much lower, than the ones observed for the Ca doped samples. The perovskite structure (peaks labelled "P") stayed intact at all measured temperatures.

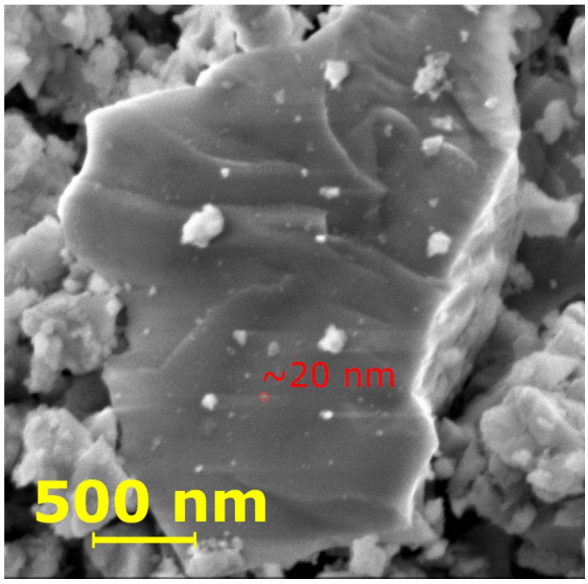

Figure S13 SEM image of the LSF-sample after reduction in wet H_2 at 500 °C, collected at an accelerating voltage of 5 kV. Small exsolved nanoparticles with diameters of around 20 nm decorate the perovskite surface.

S8. References

NIST *Chemistry, WebBook , SRD 69,* https://webbook.nist.gov/cgi/cbook.cgi?ID=C7732185&Units=SI&Mask=1#Thermo-Gas.